The Astrophysical Journal, 853:12 (15pp), 2018 January 20 https://doi.org/10.3847/1538-4357/aa9e8e
© 2018. The American Astronomical Society. All rights reserved.

Transition Elements in Supernova Presolar Grains: Condensation versus Implantation

Kuljeet K. Marhas[1] and Piyush Sharda[2,3]
[1] Planetary Sciences Division, Physical Research Laboratory, Ahmedabad, Gujarat 380009, India; kkmarhas@prl.res.in
[2] Department of Physics, Birla Institute of Technology and Science, Pilani, Rajasthan 333031, India
[3] Department of Electrical and Electronics Engineering, Birla Institute of Technology and Science, Pilani, Rajasthan 333031, India
Received 2017 October 2; revised 2017 November 28; accepted 2017 November 28; published 2018 January 17

Abstract

We compute the concentrations of five transition elements (Cr, Fe, Co, Ni, and Zn) via condensation and implantation in supernova presolar grains (Silicon Carbide Type X) from the time they condense until the end of the free expansion (or pre-Sedov) phase. We consider relative velocities of these elements with respect to grains as they condense and evolve at temperatures $\lesssim$2000 K; use zonal nucleosynthesis yields for three core collapse supernovae models $-15\,M_{\odot}$, $20\,M_{\odot}$, and $25\,M_{\odot}$; and use an ion target simulator SDTrimSP to model their implantation onto the grains. Simulations from SDTrimSP show that maximal implantation in the core of the grain is possible, contrary to previous studies. Among the available models, we find that the $15\,M_{\odot}$ model best explains the measured concentrations of SiC X grains obtained from the Murchison meteorite. For grains where measured concentrations of Fe and Ni are $\gtrsim$300 ppm, we find the implantation fraction to be $\lesssim$0.25 for most probable differential zonal velocities in this phase, which implies that condensation is more dominant than implantation. We show that radioactive corrections and mixing from the innermost Ni and Si zones are required to explain the excess Ni (condensed as well as implanted) in these grains. This mixing also explains the relative abundances of Co and Ni with respect to Fe simultaneously. The model developed can be used to predict concentrations of all other elements in various presolar grains condensed in supernova ejecta and compared with measured concentrations in grains found in meteorites.

Key words: circumstellar matter – dust, extinction – nuclear reactions, nucleosynthesis, abundances – supernovae: general

1. Introduction

Supernovae (SN) are rare astronomical events (~3 per century) that provide an enormous wealth of information on stellar evolution and nucleosynthesis of elements. Studying these singular events has been quite challenging, given the large scale of energies (10^{51} J), mass (~10–200 $M_{\odot}$), and temperatures (~10^9 K) involved in supernovae physics. As the matter moves outward after an SN explosion, expanding envelopes of stellar ejecta cool adiabatically. Eventually, the condensation of solid grains of sizes ranging from nanometers to a few 10s of microns (Goel & Murty 1982; Nuth 1988) takes place. These grains, which are found in meteorites, are termed *presolar grains*, owing to their time of formation which precedes that of the solar system (Lewis et al. 1987; Amari et al. 1990). At times, these are also referred as *circumstellar grains*, and the ones condensing around supernovae have been termed *X grains* (Amari et al. 1990, 1992) or *SUNOCONS* (Clayton 1975a, 1975b; Clayton et al. 2002). These grains not only carry imprints of the nucleosynthesis environment within the star but also provide an insight into post explosion ejecta evolution and related processes that go on in the supernovae environment (SNe).

Of the various minerals (like nitrides, oxides, carbides) condensing in the SNe, largely, silicon carbide (SiC) has been studied most in the laboratory for its morphology, along with elemental and isotopic compositions (Zinner 1998; Hoppe et al. 2010, 2014b; Liu et al. 2017). The SiC X grains from supernovae constitute ~1% of the total presolar SiC grains and are characterized by higher $^{12}C/^{13}C$ and lower $^{14}N/^{15}N$ ratios than solar abundances (Lodders & Amari 2005). In fact, few of these contain high $^{26}Al/^{27}Al$ ratios (up to 0.6), and all are consistently endowed with ^{28}Si enrichment. Supernovae genesis of these grains is strongly supported by traces of ^{44}Ti and ^{49}V, which are produced during the explosive nucleosynthesis of ^{44}Ca and ^{49}Ti, respectively (Nittler et al. 1996; Hoppe & Besmehn 2002; Amari et al. 2014), suggesting these grains condense around type II core collapse supernovae (CCSN; Amari et al. 1992), although the possibility of finding X type SiC grains in SN Ia cannot be ruled out (Clayton et al. 1997; Amari et al. 1998).

The pre-explosion SN structure can be associated with chemically distinct zones marked by the most abundant element(s) (i.e., ^{56}Ni, ^{28}Si, ^{20}Ne, ^{16}O, ^{12}C, ^{4}He, and ^{1}H), in the order of successive hydrostatic burning stages (Meyer et al. 1995). The innermost shells are rich in transition elements since the high binding energy of Fe stops further fusion. Post explosion, neutron sources (like some radioactive elements) and most abundant elements in each of these zones transcend into regions with variable abundances of certain isotopes, which are the diagnostic signature of a supernova. Extensive mixing occurs due to Rayleigh–Taylor (RT) instabilities at the zonal boundaries, due to which material from the interior is mixed with the outermost envelopes, as predicted by simulations (Kifonidis et al. 2003) and confirmed by laboratory measurements (Drake et al. 2002; Kuranz et al. 2009). Similarly, H from the outermost zone gets mixed with He and other zones in the interior in a series of reverse mixing stages because of Richtmyer–Meshkov instabilities (Borkowski et al. 1992; Kane et al. 1999). Isotopic ratios of elements can provide information on the nucleosynthesis pathways, with evolution and mixing occurring at the peripheries of various zones.

While Verchovsky et al. (1998) proposed elemental abundances to be highly sensitive to grain size as evidence for ion implantation, Marhas et al. (2006) proposed the

existence of a negative correlation between elemental concentration and grain size. To understand and relate the isotopic signatures observed in presolar grains with post supernovae RT mixing, we have constructed a model to simulate trace ion implantation in the SNe. Specifically, the simulations study high energy Cr, Fe, Co, Ni, and Zn from SN explosion interacting with 1 and 5 μm SiC grains. The model proposed can be applied to all isotopes eventually; we choose to begin with transition elements because their implantation has not been studied in detail, unlike the implantation of noble gases (Verchovsky et al. 2003, 2004; Huss et al. 2008) and low mass elements like Li and B (Hoppe et al. 2001; Lyon et al. 2007). In fact, some predictions for the rare earth elements have also been made (see, e.g., Yin et al. 2006). The idea is to de-alienate ion implantation with direct condensation and compare this with observations from laboratory studies. Incorporating RT mixing and differential zonal velocities makes the model highly versatile because one can vary these parameters to correspond with measured concentrations and the resulting parameter set can give a handle on physical conditions present in the grain surroundings at the time of implantation, not to mention the mass of the progenitor where these grains must have condensed in the first place.

We study backscattering, implantation, transmission, and sputtering (hereafter BITS) processes to check the total implantation of these isotopes in a spherical SiC grain. In Section 2, we talk about supernovae nucleosynthesis (which leads to the production of heavy ions in question) and condensation of SiC in SNe. Section 3 discusses the theory of transition ion implantation in presolar grains, and Section 4 describes how the ion target simulator SDTrimSP is set up. We present all the results and calculations in Section 5: Section 5.1 gives a summary of BITS processes and Section 5.2 lays down all the calculations by taking up the example of Cr. In the last Section 5.3, we compare our calculated concentrations with the ones measured in the laboratory, improve them by adding appropriate corrections, and discuss the reasons for similarities and discrepancies. Finally, we summarize our results in Section 6. In the Appendix, we show the derivation of the model used for studying ion transmission through the grain.

2. Nucleosynthesis and Condensation within SNe

Nucleosynthesis in CCSN has been studied in detail over the last couple of decades after major breakthroughs in computational astrophysics. Although 3D hydrodynamic models have also been developed (Utrobin et al. 2015; Wongwathanarat et al. 2015; Müller et al. 2017), they are still subject to scientific scrutiny, as the explosion mechanism is not properly understood. To explore the implantation of trace elements into presolar grains, it is vital to analyze their evolution after explosion. We use the zonal nucleosynthesis yields provided by one of the hydrodynamic models, along with the surrounding conditions to predict the amount of transition ion implantation in grains condensed in the ejecta.

There are numerous models which lay down nucleosynthesis yields from CCSN explosions (Burbidge et al. 1957; Woosley & Weaver 1986, 1995; Thielemann et al. 1996; Heger & Woosley 2002, 2010; Rauscher et al. 2002; Kobayashi et al. 2006; Nomoto et al. 2006; Woosley & Heger 2007; Pignatari et al. 2015; Sukhbold et al. 2016). In this work, we utilize the zonal yield sets from Sukhbold et al. (2016; hereafter, S16), which used the modified 1D hydrodynamic code KEPLER[4] along with P-HOTB. P-HOTB stands for Prometheus-Hot Bubble and was used to study core collapse (Janka & Mueller 1996; Kifonidis et al. 2003), whereas KEPLER was used to evolve the star along zero age main sequence and calculate nucleosynthesis yields and light curves (Weaver et al. 1978). For models that exploded, isotopic yields were generated post explosion. The zonal yields were obtained for three particular models, 15.2 $M_\odot$, 20.1 $M_\odot$, and 25.2 $M_\odot$, $\sim$200 s after the explosion, before any mixing could take place.[5] Although all models in S16 data set assume solar metallicity and do not take into account the effects of rotation, they can account for (1) detailed neutrino transport calculations using an improved explosion mechanism, as compared to Rauscher et al. (2002) and Woosley and Heger (2007); (2) a central engine that considers matter inside the collapsed core, unlike certain other models that investigated only the matter exterior to the central engines used; and (3) unlike previous nucleosynthesis models, all models[6] used here are not exploded by injecting artificial energy because (a) models below 15 $M_\odot$ almost always explode, (b) models in 20–30 $M_\odot$ rarely explode, and (c) most models above 30 $M_\odot$ implode and become black holes (see Figure 14 in S16 for the probability of explosion of different progenitor masses). In fact, the few models above 30 $M_\odot$ in which explosion does take place is due to their core being ripped apart by winds to sizes comparable to $\sim$15 $M_\odot$. The decimals in the progenitor masses of these models might seem bizarre; the reason is that the authors have tried to explode all possible progenitor masses in steps of 0.1 $M_\odot$ between 12 and 30 $M_\odot$; however, 15.0, 15.1, 20.0, 25.0, and 25.1 $M_\odot$ imploded in their simulations. This apparently small change in progenitor mass, which leads to an altogether different end scenario, is due to small but significant variations in the progenitor compactness (O'Connor & Ott 2011) rather than the central engine characteristics (Pejcha & Thompson 2015). This effect is more pronounced near progenitor masses of $\sim$20 $M_\odot$ because the carbon burning stage changes to the radiative pathway from a convective mechanism. In fact, it has been recently shown that two similar progenitors with identical masses but slightly different input physics can lead to totally different scenarios (Sukhbold et al. 2017). Thus it is not unusual for such stark differences to show up between two similar progenitor stars. Throughout this paper, we frequently approximate 15.2–15, 20.1–20, and 25.2–25 $M_\odot$ models for the sake of simplicity.

SiC condensation could have taken place either in the inner shell or in the outer He shells where zonal C/O $>$ 1 (Larimer & Bartholomay 1979; Lodders & Fegley 1997). The inner shell where ^{4}He is thought to be the most abundant isotope is negligible in size as compared to its neighboring shells, for the three models in consideration. In fact, we only observe a clear ^{4}He dominated shell in the 25.2 $M_\odot$ explosion model. Nevertheless, in the inner region, SiC condensation can be more prevalent in large progenitor mass models (like the 25.2 $M_\odot$ model) having more energetic explosions, provided the temperature is brought down to $\sim$2000 K within a few hundreds of days, because at $T > 2000$ K, SiC is assumed to be stable only in its molecular form and does not condense to form a grain (Sarangi & Cherchneff 2013). The SiC grains

[4] https://2sn.org/kepler/doc/Introduction.html
[5] T. Sukhbold (2017, private communication).
[6] Each model has a particular progenitor mass.

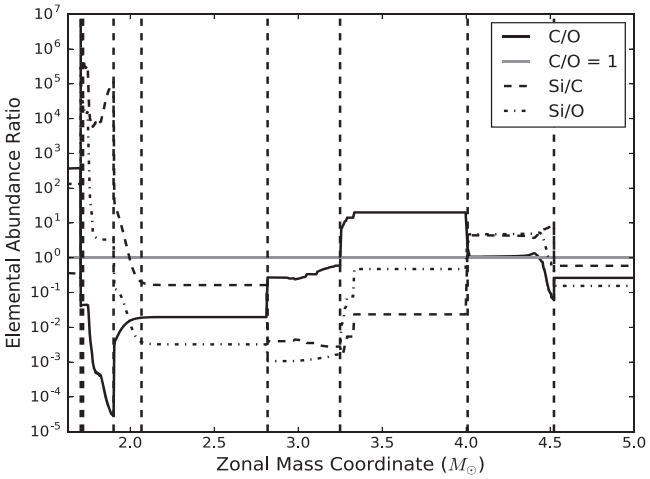

Figure 1. Semi-logarithmic plot showing the variation of C/O, Si/C, and Si/O with zonal mass for a 15.2 $M_\odot$ model. We also show a reference line for C/O = 1. Vertical dotted lines mark zones classified by most abundant elements: Ni, Si/S, O/Si, O/Ne, O/C, He/C, He/N, and H, respectively. C/O > 1 in the He/C and He/N zones, which have the highest probability of SiC formation. This ratio sharply decreases to ∼0.8 and then to ∼0.014 in the inner regions but remains essentially constant for the outer H and He envelopes. We only plot the figure until a zonal mass coordinate of 5.0, after which the ratios remain constant throughout the H zone.

formed in the inner region (if any) are, however, prone to destruction due to excessive sputtering by ions present in the nearby O rich regions or due to scattering by high energy particles. Moreover, TiC and SiS have been found to be more stable condensates in the inner regions where C/O < 1, rather than graphite or SiC (Ebel & Grossman 2001; Sarangi & Cherchneff 2013). Thus we do not study SiC condensation in the inner regions and focus only on the outer He rich zone. However, Clayton et al. (1999) have argued against the limiting criterion of C/O > 1 by proposing the formation of large (up to few μm) C grains in the ejecta interior if CO molecules are destroyed by radioactive nuclei early on and C atoms are freed. Notwithstanding such evidence for the formation of SiC, we have considered SiC condensation in an environment where C/O > 1. These regions can be identified in the mass fraction plot against the mass of the star, as shown in Figure 1 for a 15.2 $M_\odot$ model to be between 3.2 and 4.0 $M_\odot$. Similarly, we obtain the C/O > 1 regions as 5.0–6.1 $M_\odot$ and 7.2–8.2 $M_\odot$ for 20.1 $M_\odot$ and 25.2 $M_\odot$ models, respectively. Typically quoted condensation temperatures for SiC in this zone are $\leqslant$2000 K (Lattimer et al. 1978; Lattimer & Grossman 1978; Lodders & Fegley 1995), which are similar to those predicted for the solar neighborhood, in spite of the lower pressure present in SNe due to the depletion of hydrogen (except for in the outer H shell; see Grossman & Fedkin 2013).

Observations of expanding envelopes of supernova ejecta suggest grain condensation can occur as early as 300–600 days (Kozasa et al. 1989; Wooden 1997; Nozawa et al. 2003). A recent work by Trappistch et al. (2017) highlights a similar condensation time for Sr, Zr, and Ba isotopes found in presolar SiC X grains. On the other hand, a much delayed formation (later than 1100 days) is proposed by Sarangi and Cherchneff (2015) in the outer region after explosion for a 15 $M_\odot$ stellar model, owing to (1) the presence of He^+ (the presence of which will not let temperature decrease below 2000 K; see also Lepp et al. 1990) for the first 1000 days after the explosion and (2) more efficient rates of condensation for carbon dust than SiC (Cherchneff & Dwek 2009). Further, they also predict that SiC condensation starts as late as ∼1740 days, for a homogeneous ejecta model for a 19 $M_\odot$ star. An earlier condensation (∼900 days) can be achieved if one takes into account the clumpy model, which says that the ejecta is no longer homogeneous after a few hundred days and is separated into spherical clumps owing to the fingerlike projections generated due to RT instabilities (Chevalier et al. 1992).

After explosion, the immediate major source of heat present is in the form of high energy radioactive elements, and condensation can start quite early in regions where such materials are in scarcity. In the inner regions, the subsequent presence of γ-rays and Compton electrons (Clayton et al. 2001; Deneault et al. 2006) is detected, which ionize all material they encounter, and hence the ejecta attains very high temperatures (∼10^6 K or more). In addition, the presence of UV radiation due to the degradation of γ-rays can also cause the destruction of grains, although its effect is not as pronounced as that of Compton electrons (Cherchneff & Dwek 2009). The reverse shock while traveling inward also tends to heat the ejecta and reaches the remnant core by the end of the free expansion phase (also called the pre-Sedov phase; Spicer et al. 1990).[7] Its effect on SiC condensation is not clearly understood.

C > O could also lead to some of the C being tied up as CO, thus delaying the formation of SiC; unless radioactive ions like ^{56}Co can dissociate CO and free C atoms over a timescale of months, as suggested by Clayton et al. (2001) and Yu et al. (2013). However, the radioactive ions carry heat with them; thus their presence could increase the temperatures to more than 2000 K (Nadyozhin 1994; Wongwathanarat et al. 2017). In O rich regions, SiO formation is more efficient and thus preferable to SiC; however, its total mass strongly decreases from its initial value at 200 days to that at 1500 days (Sarangi & Cherchneff 2013). It is also believed that SiO is the starting molecule in the formation of SiC. This is in direct support of an often quoted larger value of Si/C, since if Si $\gg$ C, SiC condensation can be straightforward because even after some Si atoms are locked in by O in the form of SiO, enough Si can be present to get condensed to SiC. A recent study by Deneault (2017) shows a direct dominance of the radiative formation of SiC over SiO in the outer He rich zones. This is also confirmed by ALMA observations of SN1987A (Matsuura et al. 2017), where the authors find only 10% of the total Si synthesized in SNe to be locked up in SiO. In addition, the authors also report a deficiency of SiS as compared to theoretical models (Sarangi & Cherchneff 2013), whose overproduction could decrease the availability of Si for SiC. The grain formation rate first increases as the temperature cools down, and then it decreases as the concentration of key species decreases.

Overall, condensation of SiC primarily depends on the temperature of the ejecta and the concentration of the key species. To demonstrate our calculations, we consider SiC condensation as late as 1700 days after explosion, in line with the recently proposed kinetic model of SiC formation by Deneault (2017). By this time, the temperatures in the He zones

[7] The term "free expansion phase" refers to the initial few hundred years after an SN explosion, where the ejecta moves outward with negligible deceleration. It is also called the pre-Sedov phase. This term is not really accurate, because a reverse shock already starts traveling inward during this phase, which can heat the material it encounters to X-ray emitting temperatures.

are in the order of a few hundred K (Sarangi & Cherchneff 2013). We call this *delayed condensation* because other grain species are believed to undergo condensation at earlier times (Todini & Ferrara 2001; Nozawa et al. 2003; Sarangi & Cherchneff 2015). We urge the reader to go through Grossman & Fedkin (2013) and Sarangi & Cherchneff (2013) for a full zonal sequence of condensates produced in the supernova ejecta.

3. Ion Implantation: Transition Elements in SiC Grains

Deneault et al. (2003) have described the reverse shock mechanisms that propel the grain outward in the ejecta. This model provides grain velocities of the order of a few hundreds of km s^{-1} during the first few years, wherein they take the grain velocity to be 60% that of the shock velocity. Similarly, Nozawa et al. (2006) suggest a value of 75%. This is due to the deceleration of ejecta when it collides with reverse shock and formation of a contact discontinuity (Truelove & McKee 1999). Considering these values, we have carried our simulations for ion velocities in the range 1000–6000 km s^{-1}.

We focus on 1 and 5 μm grain sizes because such grains are most probable to survive sputtering in the SNe (and later on in the interstellar medium [ISM]). Grains smaller than these sizes are highly prone to destruction within the SNe itself (Jones et al. 1994, 1996). In addition, high velocity implantation (which we study in this work) will be lesser in smaller grains, since more ions will be able to transmit through them. In fact, it has been shown that grains smaller than $\sim$0.05 μm are destroyed due to excessive sputtering, whereas $\sim$0.05–0.2 μm sized grains are trapped into a dense shell, making it impossible for them to be ejected into the ISM (Amari et al. 1995; Nozawa et al. 2007). Moreover, μm sized SiC grains condensed in SNe have been proposed to survive the SN shocks and get ejected into ambient ISM (Slavin et al. 2004). Their longer lifetime as compared to graphite is another reason put forth for explaining SiC in μm sized presolar grains (Hirashita et al. 2016). Some smaller grains are also believed to have accumulated to form a larger grain size which can ensure their survival, especially due to charge separation between the smaller and larger grain and subsequent coagulation (Horanyi & Goertz 1990). A majority of SiC grains chemically separated in the laboratory have a size of $\sim$0.1–10 μm. Lastly, we note that our choice of grain sizes is based on the comparison of our calculated concentrations with those measured through NanoSIMS by Marhas et al. (2008), where the grain sizes were of the order of a few μm. Though grain sizes as large as 50 μm have also been found in meteorites, which are believed to originate from red giant stars (e.g., Gyngard et al. 2009), SN grains have been reported to have smaller diameters (see, e.g., Ávila et al. 2013, Liu et al. 2016). The largest supernova SiC grain found to date is the famous Bonanza grain, with a size of roughly 30 μm (Zinner et al. 2011).

Isotopes of Cr, Fe, Co, Ni, and Zn relevant to this study are all created during the explosive burning of Si. A material when heated to 5 billion K experiences nuclear statistical equilibrium (Meyer 1994). For a 15.2 $M_{\odot}$ star, this temperature is achieved in a radius of around 3670 km, which encloses about 2.02 $M_{\odot}$ (S16). In general, Cr is one of the products of Si burning, whereas Co, Ni, and Zn form during the alpha-rich freeze-out phase. Si burns via a series of photo disintegration reactions, producing alpha particles, which then react with the quasi equilibrium group above ^{28}Si to form Fe group elements (Wanajo et al. 2018). During explosive burning, the nuclear burning timescale and the hydrodynamic timescales eventually become comparable, so the ejecta cools and expands before the alpha particles released from initial photo disintegration manage to get captured (thus called alpha-rich freeze-out). These alpha particles eventually get assembled to heavier nuclei on a hydrodynamic timescale, to produce elements like Ni and Zn (Saio & Nomoto 1988) within seconds of the explosion.[8] After 2.02 $M_{\odot}$, the O rich shell is present, where at temperatures ranging from 3 to 4 billion K, elements like Ca are produced. Fe is mostly produced by SNe Ia.[9]

All these ions, which are produced in the innermost shells, travel with velocities of the order of a few thousands of km s^{-1}. Grains condensing around the stellar envelopes provide a surface to stick on for these ions—analogous to cool balls in the middle of hot gas.[10] Since the grain area is quite larger than the size of particles in the gas, the rate of radiation of the grains is very large as compared to the gas particles. We discuss this transport (mixing) in detail in Section 5.3.

4. Ion Target Simulator Setup

TRIM (Transport of Ions in Matter) is a program in the SRIM (Stopping and Ranges of Ions in Matter) package, developed by Ziegler et al. (2009, 2010). TRIM was primarily used for studying implantation and backscattering in the field of materials science. It is now known that sputtering yields generated from SDTrimSP (developed by Mutzke et al. 2011; SD stands for Static-Dynamic, reflecting the fact that SDTrimSP can also work with dynamic targets, where composition of target changes as more ions are incident on it) better fits the experimental simulations than TRIM. SDTrimSP also offers a wide range of choices of input parameters, like target temperature, choice of interaction potential, and multiple bombardment of ions with varying velocities. A significant difference between TRIM and SDTrimSP arises because TRIM does not take into account the inelastic energy losses of the ions. We report calculations using implantation fraction obtained from SDTrimSP (Version 5.07). We obtain implantation data for relative velocities ranging from 1000 to 6000 km s^{-1} and perform a total of 6400 iterations per ion. This choice is motivated by (1) Vikram 100 HPC processing capabilities and (2) negligible change in statistics for iterations $\geqslant$3200.

TRIM and SDTrimSP only work for planar targets, so we extend their results to a spherical target to analyze SiC grains, because it is the simplest structure we can assume the grains possess and spherical surfaces tend to be the most stable due to least surface area. The approximation we use also accounts for grain irradiation from all directions.

Out of BITS processes, backscattering does not need a different geometrical model since the ion is not interacting with the grain's interior. Also, backscattered ions interact with the grain's outer surface for a very short time, causing only surface erosion, which can be neglected when compared with sputtering due to other incident ions. For spherical modeling of implantation profiles, we follow the method developed by Vyšinka et al. (2009). This model gives

[8] 2D simulations of core collapse supernova find a higher yield of Zn as compared to S16; see Pruet et al. (2005), Wanajo et al. (2018).

[9] Fe yields given in S16 models are calibrated to their upper bounds calculated in P-HOTB in S16, since it is underproduced in massive stars.

[10] A. Sarangi 2017, private communication.

different weights to ions incident at various angles getting implanted into the grain at diverse depths by considering the sphere as a regular polyhedron whose number of sides are decided by the number of bins of incident angles used. The weight is thus a product of the depth profile and surface area of the cross section of the grain for different angles (see Figure 2 in their paper).

For spherical modeling of transmission and sputtering profiles, we follow a different approach, whose framework and calculations are derived in the Appendix. We develop it to be coherent with the content of output data files generated in SDTrimSP. The output file provides the final position of the ion before leaving the target. Taking the x axis to be the reference, we treat the distances covered in y and z directions separately and apply the model described in the Appendix on both the axes. This model assumes that ions travel in a straight path (not necessarily parallel to the x axis) inside the grain until it is ejected out. The weights are the ratio of extra length traversed in planar targets to the total length traversed in planar targets. This extra length is the distance the ions would not be traveling if the target was spherical, since they would have been transmitted at a shorter distance. The model takes as input the last known coordinate of the ion near the grain surface and the angle of ejection. Then, assuming a straight line trajectory, it backtraces the ion to its place of origin (entrance). Based on the extra distance the ion had to travel for planar surface and the decrement in its kinetic energy inside the grain, for each ion (in the output file), we calculate the number of ions that could have been transmitted had the surface been a sphere. The straight line approximation is valid in the velocity interval where transmission dominates, since at these velocities, the ion cruises through the grain in an approximately linear trajectory. We confirm this by tracking ion trajectories throughout the target and find them to be approximately linear. This provides reasonably good results, considering the weights are applied to each ejected species individually, which is different from the model described for implantation, where weights are applied in chunks decided by the bin size. Following the notations given in the Appendix, we note that $L_p/L_{\rm sph} > 1$, where L_p is the length on planar surface and $L_{\rm sph}$ is the projected length traversed in the sphere. We assume that transmission in 1D is inversely proportional to the distance traveled and is co-dependent on the energy of the incident ion, since an ion with relatively less kinetic energy may also get transmitted if the angle of incidence is high.

Sputtering yields are highly sensitive to surface binding energies (SBE) and lattice binding energies. It is a general practice to use heat of sublimation as SBE; however, the results do not match the experimental data obtained (at energies quite lower than the one discussed in this paper), especially for strong electronegative elements like O and C, since strong ionic bonds can form between atoms in the top layer and those in the bulk (Mutzke & Eckstein 2008; Wittmaack & Mutzke 2012). We use the model developed by Kudriavtsev et al. (2005), which takes into account weighted contributions from ionic and covalent bonds to calculate SBE. We provide all analysis without considering relativistic effects which are negligible at the range of velocities in question. In subsequent sections, we frequently use the terms "larger" and "smaller" grain to refer to 5 and 1 μm grains, respectively.

5. Discussion

5.1. BITS Processes[11]

Using information from typically quoted shock and ion velocities in young supernovae (for example, Kirshner et al. 1987; Chevalier 2005; Diehl et al. 2013), we use an upper bound of 6000 km s^{-1} for transition elements' implantation in SiC. At relative velocities higher than 6000 km s^{-1} for these elements, $\sim$99.8% of ions get transmitted through the grain. The remaining $\sim$0.2% that get implanted have a major contribution from extremely oblique angles of incidences, which are mathematically possible but physically rare as compared to equatorial ion bombardments. At relative velocities lower than 1000 km s^{-1}, most ions get backscattered or are implanted into the upper surfaces of grains, which have a high probability of being lost due to sputtering and erosion. We observe that the contribution of extremely oblique angles ($>75°$) in implantation fraction is quite low ($\lesssim$1% for velocities $<$3000 km s^{-1} and $\lesssim$0.2% for velocities $>$3000 km s^{-1}). The fraction of ions backscattered decreases as incident velocity is increased to 6000 km s^{-1}. Backscattered ions incident at oblique angles undergo a maximum loss of $\sim$36% in kinetic energy, while the ions backscattered at around 45° face a maximum reduction of only 7%. Most runs did not give any backscattering for normal angles.

The low sputtering yields of Si and C by transition elements with velocities outside this range eliminate any possibilities of them significantly impacting the grain. At 6000 km s^{-1}, we find a sputtering yield of $\sim$0.06 for C and $\sim$0.08 for Si per incident transition ion, which is negligible as compared to the ones obtained in the lower energy range ($\sim$2–10 per incident ion). Maximum sputtering is observed at oblique incident angles, since at such angles more momentum transfer can take place and more atoms from the surface can be easily knocked out. Maximum damage to the grain is caused in the range of velocities showing maximum interaction (or, equivalently, implantation). Sputtering yields can go as high as $\sim$28 times while the angle of incidence is changed from 0° to 85°. For example, taking a numerical value of 20 ions sputtered per incident ion for Si (as observed in a run for Cr ions with a relative velocity of 1000 km s^{-1} at 85° angle of incidence at 300 K), we see that a total of 10^{-8}% of Si ions have been knocked out from the grain (assuming the process goes on for a few hundred years), which is still low to cause any significant changes. Also, for velocities near 1000 km s^{-1}, the sputtering yields were more at higher temperatures than at room temperature, which is a straightforward consequence of more atoms being knocked out by hotter incident ions. C has a higher sputtering yield than Si at $T \leqslant 800$ K and vice versa, irrespective of the angle of incidence, which can be attributed to the fact that lighter atoms have a higher cross section to interact with the collision cascade and are thus more easily sputtered out (see the review by Smentkowski 2000 and references therein).

We note that the sputtering effects obtained from simulations only consider sputtering by a particular ion incident on the grain and associated collision cascades, whereas in reality there can be other fast moving ions hitting the grain simultaneously. For example, the sputtering yield of O atoms on SiC is proposed to be unity (Tielens et al. 1994), which would lead to

[11] All the discussion on this subsection is with respect to a 1 μm grain, unless stated otherwise.

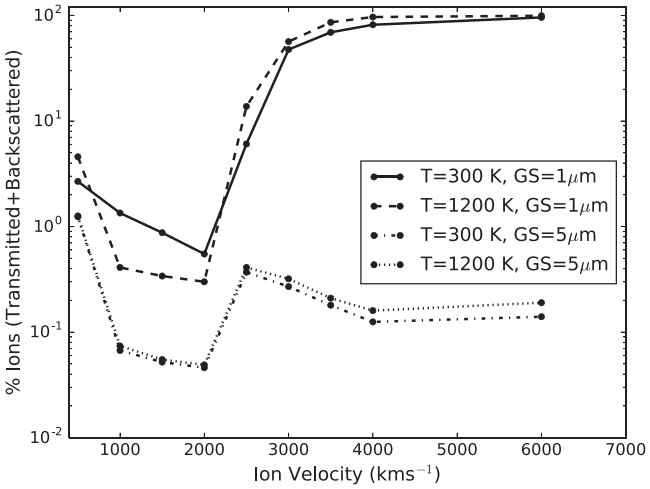

Figure 2. Percentage of Cr ions transmitted and backscattered when incident with various velocities. GS refers to the grain size. Other ions show similar trends. Trends in implantation fraction for ion velocities $\leqslant$2000 km s^{-1} in a 1 μm grain change when $T > 800$ K for Cr and Zn; however, the larger grain shows no such variations in implantation fraction for all elements. The lower velocity region ($\leqslant$1500 km s^{-1}) is dominated by backscattering and the higher velocity region (>2500 km s^{-1}) is dominated by transmission.

a significant destruction of their surface (because the abundance of O is high in nearby shells), enough to completely wipe the grains out. On the contrary, Nozawa et al. (2003) proposed a recycling scenario wherein the top 14% of the surface is recycled multiple times while it stays in the SNe. This also explains the seemingly low concentrations of O atoms found in SiC grains.[12] Although SiC grains $\gtrsim$0.1 μm can survive thermal sputtering in the remnant (Biscaro & Cherchneff 2016), they are prone to destruction due to nonthermal sputtering by He^+ (Ar^+ and Ne^+ destroy SiO and other oxides formed in O rich zones in a similar manner) present in the ejecta. However, as shown in these studies, the sputtering yields of He, D, H, and nonthermal material on SiC is lower than that of O by at least an order of magnitude, and SiC grains >0.1 μm can survive this destruction. Thus we assume a 10% surface destruction of the grains (i.e., loss of 10% of the grain's surface area), leading to the loss of ions implanted in the top 10% of the grain surface, which is also consistent with the 6%–8% surface erosion for μm sized C, Fe, and Mg_2SiO_4 grains proposed by Nozawa et al. (2007).

Transmission is the dominant phenomenon among BITS processes at ion velocities >3000 km s^{-1}. At such velocities, the interaction time of the grain with the ion is far less and the ion affects the spatial arrangement of target atoms only at highly oblique angles ($\geqslant$75°). Based on our model, we find a high increment in the number of transmitted atoms (up to 40% in certain cases) as compared to planar surfaces. Transmission is initially high at normal incident angles and is almost null beyond 70°. As the incident velocity of ions is increased, transmission of ions starts at higher angles of incidence. Figure 2 summarizes the fraction of ions transmitted or backscattered against incident ion velocities, for different combinations of temperature and grain sizes. The trends shown are consistent for all the ions in question. We see a comparatively lower fraction ($\lesssim$10%) of ions backscattered and transmitted from the grain when ion velocities are <3000 km s^{-1}. However, this shoots up to ~50% for velocities near 3000 km s^{-1} and reaches nearly unity for velocities ~6000 km s^{-1}. On the other hand, the 5 μm grain hardly shows any transmission or backscattering, and almost all the incident ions are implanted. Thus we conclude that there lies a certain range of ion velocities where implantation is dominant (~1000–2000 km s^{-1}). At velocities lower than this range, most ions are backscattered, whereas for velocities higher than this range, most of them are transmitted.

We find that BITS processes are very sensitive to ion velocity and grain size, especially if the grain is smaller (~1 μm). For velocities $\lesssim$2500 km s^{-1}, more than 90% of the ions are implanted in a 1 μm grain; for velocities between 2500–4000 km s^{-1} and >4000 km s^{-1}, 50%–80% and 90%–97% of ions are either transmitted or backscattered, respectively. We also see a drop of 7%–87% in implantation fraction at temperatures >800 K for Cr and Zn ions, while the implantation fractions for the other three elements (Fe, Co, Ni) remain independent of temperature. For Zn, this can be attributed to its volatility (the boiling point of Zn is 1180 K),[13] while for Cr, it can possibly be attributed to the formation of certain unstable complexes of Cr and C that could get evaporated at higher temperatures. These formations are highly favored if there is some O available as well, such that CO–Cr complexes can be produced (Sarkar et al. 2013). For Cr, this bias at high temperatures could also be simply due to Cr loosing its outermost electron in the $4s^1$ shell in the simulations. This would not be true for an SNe where highly ionized Cr would be present. The difference is then reflected in the final concentration estimated for these elements. For the 5 μm grain, implantation fraction remains constant for all temperatures $\leqslant$2000 K.[14]

Simulations also predict changes in the spatial arrangement of atoms in the smaller grain's core due to ion implantation, especially when the population of ions implanted near the center of the grain is highest, as shown in Figure 3, which has been reproduced from Sharda & Marhas (2017). For the larger grain, core implantation could not be achieved, even at velocities ~6000 km s^{-1}. The effect on the core, although small, is significant and addresses the question of possibility of core contamination due to implantation in presolar grains. This is contrary to an often quoted assumption where core implantation is ruled out (Deneault et al. 2003; Marhas et al. 2008). Ions implanted in the core have a higher chance of survival, and the signatures of smaller grains with sufficient core implantation can be preserved if they are embedded into bigger grains as subgrains. Thus, if an enhanced abundance of trace elements is obtained in X type grains with progenitor masses $>20\,M_\odot$, a plausible conclusion of this excess abundance can be the inclusion of subgrains within larger grains while they were still condensing. These subgrains may contain an enhanced abundance of trace elements condensed or implanted in their core, which could have survived after condensing in a bigger grain. As a matter of fact, a recent analysis has found FeS and TiC subgrains in presolar grains (Groopman 2015; Haenecour et al. 2016).

[12] Other possible explanations proposed by Nozawa et al. (2003) are the formation of O_2 or CO and diffusion through the grain.

[13] *Source:* Royal Society of Chemistry, www.rsc.org.

[14] This observation was noted by running simulations at $T = 1600$ K and $T = 2000$ K, whose results overlapped with the trends at $T = 1200$ K, as shown in Figure 2.

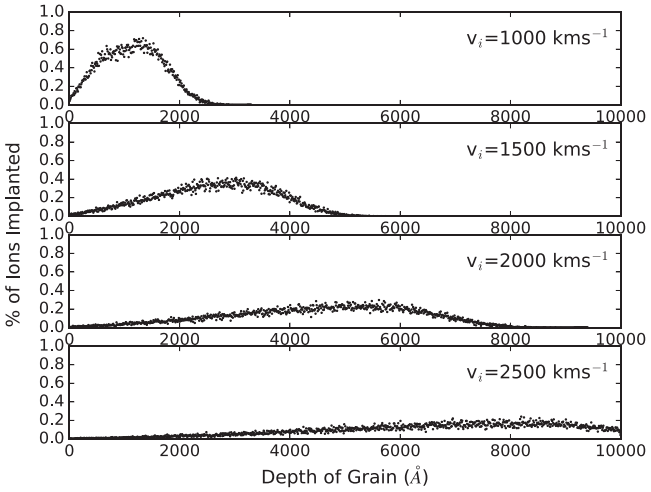

Figure 3. Depth profiles obtained from SDTrimSP simulations for Cr ion relative velocities of 1000, 1500, 2000, and 2500 km s^{-1} (subplots 1, 2, 3, and 4) incident on a μm sized SiC grain, plotted against percentage of implantation. Simulation corresponding to 2000 km s^{-1} shows maximal ion implantation in the core of the grain.

5.2. Concentration Calculations

We follow the work done by Deneault et al. (2003) for calculating the concentrations of Cr, Fe, Ni, Co, and Zn at different temperatures and velocities. The number of possible interactions that ions of a particular species in a column of uniform cross section (same as that of the grain) can have with the grain at a given time after explosion is described by

$$N_z^A = \frac{N_A \sigma}{\mu_z} \int_{m_0}^{M} \frac{X(m)dm}{4\pi r^2(m)}, \quad (1)$$

where N_A is the Avogadro's number, μ_z is the atomic weight of the element, σ is the grain cross section, r is the radial coordinate, $X(m)$ denotes the mass fraction of the isotope as a function of mass coordinate, m_0 denotes the mass coordinate at r_0 where r_0 is the grain condensation radius, and M is the total ejecta mass. Equation (1) does not consider the time expansion of ejecta. Hence we introduce an additional term where the ratio of initial to final volume of the zones where implantation can take place is derived and used as a factor to decipher the possible number of interactions at a later time t.

Early age supernovae have shock velocities of the order of a few thousand km s^{-1} (Smith et al. 1991; Borkowski et al. 2017; Sato & Hughes 2017), and the differential zonal velocities can be taken to be a substantial fraction (~60% and more) of the primary shock velocities because we consider the two outermost zones of the ejecta (He and H zones, respectively). For an estimate of final zonal widths, we consider a uniformly expanding ejecta with zones moving ahead with four possible differential zonal velocities, $(\Delta v) = 500$, 1000, 2000, and 3000 km s^{-1}, respectively.[15] We use the zonal nucleosynthesis yield model sets from S16 and apply the volume ratio factor to arrive at an estimate of number of possible interactions at times as late as a few hundred years (which marks the end of free expansion phase). To find the implantation concentration in ppm, we take its product with implantation fraction obtained using SDTrimSP at various velocities.

For a typical explosion energy of 1.327×10^{51} erg, for a 15.2 $M_\odot$, the ejecta mass as reported in S16 is 12.58 $M_\odot$, for which we obtain a radius of ~4.54 pc and the time at which the free expansion phase ends is ~431 years. Similarly, for 20.1 $M_\odot$ and 25.2 $M_\odot$ supernovae, the time marking the end of the first phase comes out as ~466 and ~458 years, respectively. Although the progenitor masses differ by ~25% for the two heavier stars considered, their free expansion phase lifetime is similar, perhaps because the stellar winds reduce the heavier star (prior to explosion) to the size same as that of the lighter star (Smartt 2009). We also observe that the ejecta mass thrown out by both stars is the same (~15 $M_\odot$), which reinforces the argument made previously.

We describe the calculations for ^{52}Cr here, at various velocities and temperatures for 1 and 5 μm SiC grains for 15.2 $M_\odot$, 20.1 $M_\odot$, and 25.2 $M_\odot$ stars, respectively. From the data for 15.2 $M_\odot$, it is observed that for a condensation radius of 1.295×10^6 km (mid-point of He zone), $X(m)$ is a constant for ^{52}Cr. The ppm concentration (by weight) is given by

$$I_c(\text{ppm}) = 10^6 I_i N_z^A \mu_z \frac{d_M^3 - d_{m_0}^3}{(t\Delta v)^3 \frac{4\pi}{3} r_{\text{SiC}}^3 \rho_{\text{SiC}}}, \quad (2)$$

where I_i is the implantation fraction of ions and is a function of ion velocity (relative to grain), grain cross section, grain density, and temperature. From a numerical integration of Equation (1) with $m_0 = 3.95$ and $M = 12.58$, for a 1 μm grain, we get $N_z^A = 1.67 \times 10^9$. Thus, for a differential zonal velocity (Δv) of 2000 km s^{-1} between zones 499 (mid-point of He zone) and 950 (last zone) in S16 zonal yield sets, at a time t (days) after explosion, the ppm concentration (by weight) is given by

$$I_c(\text{ppm}) = \frac{\beta I_i}{t^3(\text{days})}, \quad (3)$$

where β is a constant. Assuming grain condensation is fully achieved by $t = 1700$ days (Deneault 2017) and the free expansion phase ends around 430 years, we get a ppm concentration of ~0.62 for ^{52}Cr implanted in a 1 μm grain when its velocity is 1000 km s^{-1}.

So far, the mass fraction has been assumed to be constant at $t > 200$ s. However, two bipolar mechanisms can alter this mass fraction: the addition of mass into zones that are farther out as the ejecta sweeps up material from ambient ISM and the addition of mass from zones interior to the condensation zone because of RT instabilities (mixing), which are caused when a lighter fluid tends to push over a heavier fluid (discussed in detail in Section 5.3). The amount of mixing remains a largely unsettled question; however, to begin with, we consider a 1% mixing between He/C and He/N zones (as estimated by the NanoSIMS analysis of presolar grains by Marhas et al. 2008)—that is, we add 1% of the zonal yields from the He/C zone to the He/N zone while calculating implanted concentrations. The mass fraction of ^{52}Cr can increase to around double the value of $X(m)$ taken in this calculation (~83% increase in the case of ^{52}Cr implanted into SiC condensed in a 15.2 $M_\odot$ SNe). The free expansion phase ends when the SN ejecta has swept up a mass ~12.6 $M_\odot$. It can be assumed without the loss of generality that the swept-up mass that affects the mass fraction of ions in

[15] The notion of a uniformly expanding ejecta will especially not hold if the shocked material is running into denser ambient material, like molecular clouds, or is being shocked by the primary shock, cooled adiabatically, and re-shocked by multiple reverse shocks (P. Sharda et al. 2018, in preparation).

question is at least 60% of the total mass of the expanding supernova (e.g., the swept up mass of Tycho's supernova remnant [SNR] present in the outermost regions is ∼53% of the total mass of the SNR, as derived by Seward et al. 1983). Regardless, this factor is suppressed when mixing from inner regions is taken into account, as we explain in Section 5.3. It can also be safely assumed that there was no production of Cr before the explosion, and hence the swept-up mass does not contain any significant quantity of the isotope.[16] Thus the mass fraction decreases by a factor

$$\Delta X(m) = \frac{12.58 - 3.95}{(12.58 - 3.95) + (0.6 \times 12.58)} = 53.35\%. \quad (4)$$

Overall, we get a ∼30% rise in the mass fraction of Cr, which gives a corrected value of ∼0.80 ppm. In an attempt to account for grain destruction in later years in the ejecta and the ISM, we assume the loss of top 10% of the grain surface, as noted in Section 5.1. Utilizing the depth profiles obtained through spherical grain approximation for each ion implanted in the grain, we find that for this particular case, ∼59% of the ions implanted are able to penetrate the grain to more than 10% of the grain's depth. The surface erosion corrected ppm concentration thus obtained is ∼0.79 ppm. This concentration still lacks mixing from innermost zones and additional contributions from radioactive nuclei, which we correct for in Section 5.3. Interestingly, for the larger grain, most of the ions implanted are in layers deeper than the ∼10% erosion barrier threshold we work with and are hence preserved during surface erosion.

5.3. Comparison with Laboratory Measurements

The calculated concentrations of transition ions implanted in the grains vary over 1–3 orders of magnitude when ion velocities and differential zonal velocities are varied between 1000–6000 and 500–4000 km s^{-1}, respectively. However, not all the calculated values would correspond to physically plausible initial conditions, so we maintain a check on those sets, which yield erroneously high concentrations.

Laboratory measurements of these concentrations include contribution from both processes: condensation and implantation.[17] The estimates of concentrations via condensation and implantation can be matched with those measured in the grains. X type SiC grains from the Murchison meteorite analyzed in Marhas et al. (2008) have a mean size of ∼2.5 μm, with 90% sizes lying in the range 1.8–3.7 μm (Hoppe et al. 1994; Zinner et al. 2007), whereas those analyzed by Hoppe et al. (2000) have grain sizes in the range 0.5–1.5 μm. To compare the concentrations measured by Marhas et al. (2008) with our calculations, we require the implantation fraction for each incident element. We approximate it by taking a geometric mean of the resultant implantation fractions for the two grain sizes we study.

Laboratory-based ppm concentrations of Fe and Ni range from a few 10s to a few 1000s for SiC X grains found in Murchison meteorite, while those of Co are mostly a few 10s of ppm. The 15 $M_\odot$ supernova model is believed to better explain these abundances than the 25 $M_\odot$ model, as stated by Marhas et al. (2008); however, the models these authors used were taken from Rauscher et al. (2002), which have been improved upon in S16. Concentrations of Fe in smaller SiC X grains studied by Hoppe et al. (2000) lie in the range ∼100–1000 ppm. Our calculated values for Fe implanted in the grains is 0–2 orders of magnitude lesser (on average[18]) for ion velocities in 1000–3000 km s^{-1} and differential zonal velocities between 1000 and 3000 km s^{-1}. We are not aware of any measured concentrations for Zn found in presolar SiC X grains. Though Cr concentrations have been measured to be ∼1 ppm in SiC X grains (measured by Knight et al. 2008, as reported in Levine et al. 2009), we cannot utilize them since they do not belong to the same grains as analyzed by Marhas et al. (2008). Hence we leave these elements out in the discussion for comparison, but we propagate the effects of various mixing criteria we have considered in them.

Contrary to finding excess Ni in type X presolar SiC grains ($\langle$Fe/Ni$\rangle$ = 0.78 (0.14, 3.34) for the SiC X grains analyzed by Marhas et al. 2008), we find Fe/Ni > 1. Ion implantation as a probable cause for this excess was ruled out by Marhas et al. (2008), because these excesses were distributed all across the grain instead of being localized in the outermost regions and core implantation was not taken into account. This motivates us to consider mixing from the innermost regions (Si/S, Ni zones) as well, which are rich in Ni, and contributions from these regions can possibly explain the observed excess of Ni.

It has been shown that concentrations of certain isotopes of Si, Ti, and Ca obtained in laboratory measurements of carbide (Graphite and SiC) grains can only be explained if there is intense mixing between inner Si/S zones and outer He zones (Travaglio et al. 1999; Hoppe & Besmehn 2002), while the same has been postulated for explaining excess Ni obtained in these measurements (Steele et al. 2012). This can happen through Si rich jets originating from the Si zone in the interior and cutting across O rich zones, throwing material from the inner regions all the way out to He and H zones. The presence of Si rich jets owing to an asymmetric explosion (Khokhlov et al. 1999) has been often reported (Hwang et al. 2004; Grichener & Soker 2017 and references therein), which supports the theory of mixing from the innermost zones to sites of carbide grain condensation in the outer zones (Lodders 2006). These jets also cause alpha-rich freeze-out behind the energetic shock, which is essential for the production of transition elements in question (Nagataki et al. 1997; Nagataki 2000), and their presence would also constrain the mixing from intermediate O rich zones to lower values, which is necessary in order to limit the amount of O available in the grain surroundings so that C/O > 1 is preserved, O is held up in CO, and oxide formation can be suppressed. A homogeneous mixing from all zones is thus not preferred for explaining observed elemental abundances in presolar grains (Hoppe 2004).

3D simulations of mixing in the ejecta performed by Hammer et al. (2010) predict the formation of "bullets" (clumps) of $Z > 8$ elements (called Ni rich bullets in their paper), some of which are fast enough to overtake the O rich bullets and reach the outer He and H zones within the first 10,000 s of explosion. The same has been observed in

[16] The same assumption is valid for the other four ions because the contribution to their yields by the winds before explosion is negligible compared with their abundances produced after explosion (S16).

[17] While laboratory measurements from other instruments may contain errors due to sample contamination (Henkel et al. 2006; Knight et al. 2008), those from NanoSIMS are able to avoid it and have been shown to be quite accurate (Heck et al. 2006; Marhas et al. 2006).

[18] This average is the mean of concentrations measured by Marhas et al. (2008).

SN1987A (Arnett et al. 1989). This decay can take place in the innermost shell, which is moving the slowest, and as the ejecta cools adiabatically, γ-rays from this decay cause local heating that sends out a pressure wave toward the outside, thus giving rise to conditions necessary for RT mixing. 3D simulations of CCSN predict mixing to cease by $\sim 10^5$ s for a 15 $M_\odot$ star (Joggerst et al. 2010).

Keeping these studies in mind, we consider a 1% contribution (through mixing) of Ni from the Si/S zone and add contributions from those radioactive ions that may travel to outer zones along with Ni and Si rich "bullets."[19] Specifically, we trace (1) ^{52}Ni, ^{52}Fe, and ^{52}Mn for ^{52}Cr; (2) ^{56}Co, ^{56}Ni for ^{56}Fe; and (3) ^{59}Ni for ^{59}Co.[20] Among these, we neglect ^{52}Fe, ^{52}Mn, and ^{52}Ni because their zonal contributions are negligible as compared to that of their end products in the zones of interest. The half life of ^{59}Ni is $>10^4$ years, which implies that only 0.4% of ^{59}Ni has decayed into ^{59}Co by the end of free expansion phase (Rühm et al. 1994). Thus we use a 1% fraction of the decayed 0.4% ^{59}Ni from the innermost Ni zone and maintain the same fraction for all other elemental yields taken into account from this zone, so that zonal mixing is same for all elements and calculations are unbiased in every zone (i.e., elemental fractionation is not favored by ion implantation).

Consequently, we find that the concentrations of Ni in a 1 μm grain can increase by 19×, 14×, and 8× for 15.2, 20.1, and 25.2 $M_\odot$ models respectively, with respect to the concentrations calculated before this mixing is taken into account. Similarly, the concentrations of Co increase by ∼2.5× for all three models, whereas the concentrations of Cr increase by 5.2×, 2.3×, and 1.8×, respectively. Zn remains unaffected by mixing from the interior. This additional concentration for Ni is solely from mixing, whereas the increments in concentrations of Cr and Co come from mixing as well as radioactivity corrections. Contributions to ^{56}Fe from ^{56}Co do not lead to significant increments. The production of ^{56}Ni has been the focus of all supernovae nucleosynthesis models, and while it is a key factor to uncovering the mysteries of supernovae explosions (Hashimoto et al. 1989; Thielemann et al. 1990; Woosley et al. 2002; Nomoto et al. 2006; Woosley & Heger 2007; Jerkstrand et al. 2015; S16; Suwa et al. 2017), its contribution to the ppm concentrations of ^{56}Fe make Fe/Ni high ($\geqslant$1), whereas Fe/Ni < 1 has been measured in ∼73% of all the SiC X grains analyzed by Marhas et al. (2008). Thus we consider two scenarios: one where we refrain from adding significant contributions from ^{56}Ni to our calculated concentrations of ^{56}Fe and the other with taking it into account. The former is motivated by 3D simulations of supernovae explosions which predict that most of the mass of ^{56}Ni resides in two big clumps moving in opposite directions (Wongwathanarat et al. 2013). This is also in concurrence with the observed structure of SN1987A 23 years after the explosion by Larsson et al. (2016), where the authors quote that although the 3D simulation by Wongwathanarat et al. (2013) models the SNe environment a few hundred seconds after the explosion, the overall structure and spatial distribution of ^{56}Ni should hardly change in subsequent times. Similarly, the presence of bipolar ^{56}Ni jets has been detected in SN2013ej, which is strong evidence for the inhomogeneous and clumpy distribution of this isotope (Utrobin & Chugai 2017). We thus assume that the site of SiC condensation is away from these high velocity clumps of ^{56}Ni. In any case, most of these high velocity (4000–6500 km s^{-1}) ^{56}Ni ions would simply traverse the grain without significant implantation. For the latter scenario where we assume the formation site and consequent movement of SiC grains near ^{56}Ni clumps, we assume a 0.001% mixing of this isotope for the production of ^{56}Fe, in line with the work of Fassia et al. (1998), where this amount of mixing of ^{56}Ni from the innermost Ni zone to outer He zones has been used to reproduce the observed He I line in SN1995V.

However, despite the above additions from inner zones and radioactivity corrections, we fail to cover the whole range of measured Fe/Ni and Fe/Co ratios. On experimenting further with different sets of mixing, we find that a 2% mixing from the Si/S zone (instead of the 1% considered so far, keeping other mixing contributions constant) simultaneously generates the desired abundances of Ni and Co (relative to Fe) to a certain extent. To get to the lowest Fe/Ni ratios reported in Marhas et al. (2008), we find that a higher contribution ($\geqslant$4%) is required from the Si/S zone because in this zone, while ^{58}Ni is still in excess, ^{56}Ni has highly depleted from its value in the innermost Ni zone. Thus we land at our final calculated values of condensed as well as implanted concentrations for the species of interest by assuming (1) 0.004% and 0.001% contribution for ^{59}Ni and ^{56}Ni (respectively), 2% and 1% mixing from Si/S and He/C zones, and (2) 0.004% and 0.001% contribution for ^{59}Ni and ^{56}Ni (respectively), 4% and 1% mixing from Si/S and He/C zones, for a SiC X grain formed in the He zone. We summarize the relative abundances obtained by modeling implantation+condensation in Table 1 for the two scenarios put forth. The difference between the two scenarios can be attributed to SiC grains condensing and evolving near or far from Si rich ejecta present in the outermost layers. However, since the condensation of SiC is highly favorable if Si rich clumps (ejected outward from inner Si rich regions; see Figure 1 where Si/C $\gg$ 1) are present, scenario 2 seems more probable. Thus mixing from inner zones can also provide an explanation for the high isotopic abundances of Si in SiC X grains. If the percentage of mixing is increased by 2× in either the Ni or the He zones, it leads to an overproduction of elemental abundances by implantation itself, without leaving room for condensation. On the other hand, the concentrations decrease by 40% when mixing is taken to be 0.5% in He/C zones, which can be considered a lower threshold, since a value less than this will not produce enough abundance through implantation in the grains.

During the first few hundred years after explosion, the differential zonal velocity between He and H zones is of the order of a few thousand km s^{-1}. Thus the majority of implantation during the free expansion phase should come when $\Delta v > 1000$ km s^{-1}. There is a possibility of higher differential zonal velocities than considered in our work, but they would not exist for a long time (as compared to the timeline of few hundred years we use). Also, their contribution to the implanted concentrations would be scarce as compared to the ones considered in our calculations. We also consider a case with $\Delta v = 500$ km s^{-1}; however, the concentrations we calculate are higher than measured in more than 80% of the grains, which leads us to reject this set in most comparisons. With this

[19] This is unlike the algorithm used by Yoshida (2007) to explain observed isotopic ratios (of same elements) in SiC X grains by manipulating mixtures from different zones according to each individual grain.

[20] See National Nuclear Data Centre, Brookhaven National Laboratory's website for details on decay times and decay cascades: https://www.nndc.bnl.gov/ensdf/.

Table 1
Relative Elemental Abundances (with Respect to Fe) Calculated in This Work with Contributions from Both Implantation and Condensation Compared with Experimental Results

Elements	Solar[a]	Experimental	15.2 $M_\odot$	20.1 $M_\odot$	25.2 $M_\odot$
			Si/S Zone Mixing = 2%		
Fe/Cr	66.0	⋯	14–26	44–76	41–70
			18–34	49–86	45–77
Fe/Co	362.9	31 (3–80)[b]	32–84	76–200	58,153
			41–112	89–141	70–187
Fe/Ni	17.8	0.8 (0.1–3.3)[b]	0.90–1.03	1.43–1.61	1.6–1.8
			1.24–1.34	1.51–1.68	1.74–1.97
Fe/Zn	690.9	⋯	790–834	2098–2215	1282–1353
			1017–1073	2342–2517	1425–1657
			Si/S Zone Mixing = 4%		
Fe/Cr	66.0	⋯	15–29	46–83	43–74
			21–39	53–111	49–96
Fe/Co	362.9	31 (3–80)[b]	35–92	81–227	62–161
			47–129	94–231	69–185
Fe/Ni	17.8	0.8 (0.1–3.3)[b]	0.40–0.50	0.77–0.87	0.91–1.03
			0.63–0.69	0.84–0.99	1.04–1.13
Fe/Zn	690.9	⋯	869–917	2218–2435	1371–1467
			1170–1234	2584–2738	1574–1790

Notes. Values in column 3 are averages of the relative abundances measured in different grains, with the lowest and highest relative abundances shown in parentheses. The table is divided into two parts that show relative abundances when 2% and 4% mixing is considered from the Si/S zone, respectively. For each of these parts, values in the first row denote the maximum and minimum ratios obtained when yields from ^{56}Ni are not added to ^{56}Fe, whereas those in the second row denote relative abundances when this yield is taken into account.
[a] Lodders (2003).
[b] Marhas et al. (2008).

view, we find a probable range of fraction of abundances implanted in the SiC X grains for which ppm concentrations of Fe, Co, and Ni have been measured by Hoppe et al. (2000) and Marhas et al. (2008).

In Tables 2 and 3, we present the maximum fraction of these elements that can come from implantation when zonal mixing from the Si/S zone is 2% and 4%, respectively, by taking the geometrical mean of the implanted concentrations we find for the two grain sizes (since the average size reported in the analysis of SiC X grains is $\sim$2.5 μm). We reject certain sets that show an implantation fraction >1 for all combinations of parameters, and we call the case "NP" (not possible). For grains that show lesser concentrations, we assume they have been ejected into the ISM earlier than others. By "early" ejection, we imply that the grain gets out of the reach of high velocity ions in the shocked ISM earlier than its expected ejection time into ambient ISM. This "early" ejection scenario is possible if the SiC grain condenses near Si rich ejecta clumps moving outward at high velocities, because such clumps can cross the forward shock and move ahead of it, essentially imitating an early ejection. As a matter of fact, Si rich clumps have been observed to be moving ahead of the forward shock in the Vela CCSN (García et al. 2017). However, this mechanism requires stark density contrasts between the clump and its surroundings. Also, the time it takes for the clump to overtake the forward shock is not known with surety (see also Kundt 1988; Aschenbach et al. 1995). Another way the early ejection could be achieved is through the presence of a huge shock wave that accelerates the dust and not the gas around it. However, the origin of such a shock wave remains unclear. Thus for such grains we only consider implantation at the earliest epochs when differential zonal velocities were the highest. To explain higher concentrations, we subsequently include contributions from lower differential zonal velocity sets while assuming that these grains spent a longer time in the SNe.

As is seen from Tables 2 and 3, implantation fraction predicted for these elements covers the whole range from 0–1, depending on the physical conditions present in the SNe. If we were to believe that implantation should not contribute more than 60% (the highest predicted implantation fraction for heavy elements; Verchovsky et al. 2004) to the total concentration of transition elements found in the grain, it would imply that most of the ions are implanted in the free expansion phase when Δv is still a few thousand km s^{-1}. Since the shock velocities are of the order of a few thousand km s^{-1} in this phase, the argument made previously supports using $\Delta v > 1000$ km s^{-1} as the most probable differential zonal velocities, because at one end of it, we have nothing but the shock velocity (since we deal with the outermost layers of the ejecta). Moreover, we observe that there is almost always a steep decline in implantation fraction as one moves from a zonal velocity of 1000 to 2000 km s^{-1}. Since this decline does not seem continuous, it becomes straightforward to demarcate a maximum possible implantation fraction for the elements we study in SiC X grains.

Thus if we only take into account $\Delta v > 1000$ km s^{-1}, the implantation fraction we get is $\lesssim$0.25 for grains condensed in 15 $M_\odot$ model, where measured concentrations of Fe and Ni are $\gtrsim$300 ppm. For lower concentrations of Fe and Ni, this fraction could reach as high as $\sim$60%, while for measured concentrations $\gtrsim$1000, this fraction drops below 0.1, implying condensation is the dominant process among the two unless the grain did not spend much time in the SNe, as postulated earlier. The model also predicts that if these SiC grains were synthesized in heavier stars ($\geqslant$20 $M_\odot$), they would have spent a lesser effective time in the SNe, or the zonal velocities would have been higher in the free expansion phase. Although we

Table 2
Measured ppm Concentrations from Marhas et al. (2008) and Proposed Maximum Percentage of Ion Implantation, Unless the Maximum is 100%, in which Case the Minimum Percentage Is Shown

Element	$Conc_{measured}$	Δv	% I_{max} 15 $M_\odot$	% I_{max} 20 $M_\odot$	% I_{max} 25 $M_\odot$	Element	$Conc_{measured}$	Δv	% I_{max} 15 $M_\odot$	% I_{max} 20 $M_\odot$	% I_{max} 25 $M_\odot$
Fe	⩽50	3000	75	NP	NP	Co	⩽20	1000	58	⩾81	NP
			96	NP	NP			2000	7	24	⩾43
	50–150	2000	62	NP	NP			3000	2	7	30
			78	NP	NP		25–70	500	⩾56	NP	NP
	50–150	3000	14	⩾78	NP			1000	17	55	NP
			32	⩾85	NP			2000	2	7	29
	150–310	2000	40	NP	NP			3000	0.6	2	9
			52	NP	NP		200–220	500	42	⩾59	NP
		3000	12	93	NP			1000	0.5	17	73
			15	⩾59	NP			2000	0.6	2	9
	310–640	1000	⩾64	NP	NP			3000	0.1	0.6	3
			NP	NP	NP	Ni	⩽100	2000	⩾52	NP	NP
		2000	20	⩾62	NP			3000	37	⩾77	NP
			25	NP	NP		100–250	2000	50	NP	NP
		3000	6	45	NP			3000	15	73	⩾59
			7	70	NP		250–600	1000	70	NP	NP
	900–1100	1000	91	NP	NP			2000	21	⩾43	NP
			⩾48	NP	⩾50			3000	6	31	89
		2000	11	89	NP		650–900	1000	⩾47	NP	NP
			14	⩾56	NP			2000	14	68	⩾84
		3000	3	26	85			3000	4	20	60
			4	41	NP		950–1200	1000	83	NP	NP
	1100–1800	1000	56	NP	NP			2000	10	81	⩾63
			72	NP	NP			3000	3	24	45
		2000	7	54	⩾71		1300–1700	1000	59	NP	NP
			9	85	NP			2000	7	57	44
		3000	2	16	52			3000	2	17	32
			3	25	75		2000–2500	1000	40	NP	NP
	2000–3000	1000	33	NP	NP			2000	5	39	71
			43	NP	NP			3000	1	12	21
		2000	4	32	⩾43		∼3000	1000	33	NP	NP
			5	51	62			2000	4	32	60
		3000	1	10	31			3000	1	10	18
			2	15	45		∼3300	1000	30	NP	NP
	∼3500	1000	29	NP	NP			2000	4	29	54
			37	NP	NP			3000	1	9	16
		2000	5	28	90		∼4500	500	⩾74	NP	NP
			5	44	53			1000	22	⩾70	NP
		3000	1	8	27			2000	3	22	40
			1	13	39			3000	0.8	6	12
	∼4500	500	⩾73	NP	NP		∼5400	500	⩾62	NP	NP
			⩾93	NP	NP			1000	18	⩾59	NP
		1000	22	⩾70	NP			2000	2	18	33
			29	NP	NP			3000	0.6	5	10
		2000	3	22	70						
			4	34	41						
		3000	0.8	6	21						
			1	10	30						

Note. Mixing set used is 0.001% and 0.004% (for ^{56}Ni and ^{59}Co) from the Ni zone, 2% from the Si/S zone, and 1% from the He/C zone. Δv denotes differential zonal velocities (in km s^{-1}) between the He and H zones. For the three supernovae models for ^{56}Fe, values in the first row denote the maximum implantation fraction obtained when yields from ^{56}Ni are not added to ^{56}Fe, whereas those in the second row denote the maximum fraction of ions implanted when this yield is taken into account. When the implantation fraction >1 for all parameter sets in a model, the model is marked "NP" (not possible). For the largest measured concentrations, the sample size is 100%; hence no appropriate groups of measured concentrations could be made. Grain size has been assumed to be ∼2.4 μm. As long as $T \leqslant 2000$ K, implantation in Fe, Co, and Ni remains independent of temperature.

assume fixed zonal velocities throughout this phase, one can achieve more accuracy in concentrations by taking appropriate fractions of each zonal velocity yield. In most cases, for identical conditions, the implantation fraction of Ni is thought to be more than Fe, which makes sense because Ni is more volatile than Fe, so the condensation fraction for Fe should be higher if the same amounts of Fe and Ni condense with the grain.

Concentration of other two elements, Cr and Zn, is relatively lower—of the order of 1 and 0.1 ppm for a 15 $M_\odot$ model, 10 and 0.3 ppm for a 20 $M_\odot$ model, and 40 and 3 ppm for a 25 $M_\odot$ model. A substantial amount of Zn found in SiC X grains

Table 3
Same as Table 2, but Zonal Mixing from Si/S Zone Is Increased to 4%. The Only Significant Impact Is Caused on Implantation Fractions of Ni (Those of Fe Increase by ∼8% while They Do Not Change for Cr, Co, and Zn)

Element	$\text{Conc}_{\text{measured}}$	Δv	% $I_{\max}$ 15 $M_\odot$	% $I_{\max}$ 20 $M_\odot$	% $I_{\max}$ 25 $M_\odot$
Ni	⩽100	3000	⩾35	NP	NP
	100–250	2000	⩾47	NP	NP
		3000	33	96	NP
	250–600	2000	47	86	NP
		3000	14	55	NP
	650–900	2000	31	83	⩾84
		3000	9	36	⩾
	950–1200	1000	⩾79	NP	NP
		2000	23	⩾53	NP
		3000	7	48	93
	1300–1700	1000	⩾56	NP	NP
		2000	16	78	⩾69
		3000	5	31	50
	2000–2500	1000	90	NP	NP
		2000	11	62	⩾47
		3000	3	29	34
	∼3000	1000	75	NP	NP
		2000	9	74	93
		3000	3	27	28
	∼3300	1000	68	NP	NP
		2000	9	67	85
		3000	3	39	25
	∼4500	1000	50	NP	NP
		2000	6	47	62
		3000	2	21	19
	∼5400	1000	42	NP	NP
		2000	5	51	52
		3000	2	47	16

Note. Some sets that were included in Table 2 have been removed since all models were termed NP.

should come from implantation and not condensation because of its volatile nature, hence making it difficult to co-condense with the grain. On the other hand, Cr is refractory, so a substantial amount of it can also come from condensation. These elements will be discussed in detail in a future work, wherein measured concentrations from other X type grains will be available. We also leave calculations for Ti and V (whose ppm concentrations have been measured in presolar grains by Kashiv et al. 2001, 2002) for a future work.

A similar analysis (as we perform in this work) was recently carried out by Kodolányi et al. (2017), where the authors measured concentrations of Fe and Ni isotopes in SiC X grains obtained from KJD (Amari et al. 1994) and Mur2012B (Hoppe et al. 2014a) grain separates of the Murchison meteorite. Although they find Fe/Ni concentrations in different SiC X grains to vary more than two orders of magnitude (from 0.36 to 37.6), their measurements are doubtful due to possible contamination from multiple phases during sample preparation, because the grains they analyzed were smaller and their diameter was comparable to the beam diameter of the desorption laser used. Keeping this in mind, the authors further discussed the concentrations of only three particular grains that they expected to be least affected by contamination (see Section 4.2 in their paper). The first of these belonged to the KJD mount, whereas the other two belonged to the Mur2012B mount. Furthermore, the sizes of these three grains are between ∼0.5 and 1.0 μm, similar to the ones we have simulated. For these three grains, the authors attempted to establish links with CCSN nucleosynthesis models through a variety of mixtures of elements from different zones. The nucleosynthesis models they used were from Rauscher et al. (2002) and Pignatari et al. (2015), where the latter model included ingestion of abundances from the outermost H zone. However, they were not able to reproduce the desired abundances of all the isotopes while maintaining C/O > 1 from either of these models, for two of the three grains. On comparing the Fe/Ni ratios they find for the three grains (0.36, 1.26, and 1.24, respectively), we immediately see that we are able to reproduce the measured Fe/Ni ratios in them using the same nucleosynthesis model (15 $M_\odot$ and mixing criteria we have considered for grains analyzed in Marhas et al. 2008; see Table 1). This is encouraging and highly expected because the grains belonged to the same meteorite. Thus it is logical to argue that the grains embedded in different parts of the same meteorite originated from the same CCSN.

6. Summary

We have developed a theoretical model to estimate the fraction of transition elements condensed and implanted in SiC X grains and compared it with the concentrations obtained from SiC X grains found in the Murchison meteorite. For this calculation, we analyzed ion-grain interactions at various sets of relative velocities, zonal velocities, and temperature using an ion target simulator SDTrimSP. We use nucleosynthesis zonal yield sets generated by S16 for 15, 20, and 25 $M_\odot$ stellar models. We also take into account the time expansion of ejecta through the free expansion phase and associate appropriate radioactive corrections with our analytical calculations. This model is fairly versatile due to its two degrees of freedom (namely, ion velocity and differential zonal velocity) and can be applied to calculate implanted concentrations of all other elements (and respective isotopes) in the X grains condensed in SNe for all types of progenitor masses. Our main conclusions are as follows:

1. Backscattering is only effective for lower ion velocities ($v < 1000\,\text{km s}^{-1}$) and highly oblique angles. Only $\lesssim$6% of the ions incident are backscattered for the range of velocities we consider in this work. Using our geometric model described in Appendix, we find transmission to dominate implantation for ion velocities $>4000\,\text{km s}^{-1}$ for SiC grains of size 1 μm. Maximum transmission is ⩽10% for velocities ⩽2500 km s^{-1}, after which it shoots up to >50%, reaching almost unity for $v > 4000\,\text{km s}^{-1}$. We also confirm that sputtering of Si and C atoms by transition elements is largely ineffective.
2. While the implantation of transition elements remains fairly independent of temperature (provided $T \leqslant 2000$ K) for Fe, Co, and Ni, it decreases by more than half at $T > 800$ K for Cr and Zn. For Zn, it could be attributed to its volatility, while for Cr, it is possibly due to simulations using nonionized Cr or due to the formation of certain complexes of Cr–C that can escape out. The implantation fraction also decreases by half as relative velocities cross the $3000\,\text{km s}^{-1}$ threshold and transmission becomes dominant. Almost all the concentration of Zn found in SiC X grains can be attributed to implantation since it is volatile and any quantity of Zn

co-condensed with SiC while grain condensation is highly likely to get evaporated. Maximum ppm concentrations of Zn predicted to be implanted in a 1 μm grain are $\sim$1, 3, and 13 for 15, 20, and 25 $M_{\odot}$, models respectively. We also find that for a 5 μm grain, even though less ions get implanted in it due to its larger size, lesser ions getting lost due to surface erosion is another factor that leads to a higher concentration of implantation for the larger grain. This happens because most ions are implanted into a "penultimate" layer of the grain, at a depth below the outermost surface which gets eroded.

3. We also establish that transition ion implantation in the core of the grain is possible for a suitable range of velocities, thus increasing the chances of survival of transition elements in the grains. This is contradictory to the assumptions made so far about negligible impacts of ion implantation in the grain's core and encourages the hypothesis of smaller grains (rich in certain elements) to be embedded into bigger grains later on as subgrains. Implantation is inhomogeneous and localized, as opposed to condensation which is fairly homogeneous; however, it is more difficult than previously thought to observe this localization, because all grain regions are within the reach of implantation, specially for smaller grains ($\lesssim$1 μm). Hence the measured concentrations that vary over three orders of magnitude reflect nonnegligible weightage from varied exposures to ion implantation scenarios in the SNe.
4. We find that the observed relative abundances (due to implantation and condensation) of Fe, Co, and Ni can only be explained by considering mixing from the innermost Ni and Si/S zones and are best matched against concentrations calculated for the 15 $M_{\odot}$ model. We find the mixtures we use to agree well with measured concentrations of Fe and Ni in SiC X grains from different mounts of the Murchison meteorite. In addition, the S16 model confirms that such a mixing can also explain the isotopic abundance of Si in SiC X grains. This is in sync with 3D simulations and subsequent observations of SNRs which conclude that mixing happens as early as after a few 10s of seconds and ceases near $\sim 10^{5-6}$ s. We work with two sets of mixtures from the Ni, Si/S, He/C, and He/N zones, and follow two scenarios (for each mixture) for the role of ^{56}Ni in the implantation of ^{56}Fe, owing to its inhomogeneous distribution in the form of clumps. Mixing from the Si/S plays the most important role in calculating the concentrations of Ni and Co. In addition, mixing from the He/C zones cannot be as high as 5% or as low as <0.5% in order to explain the measured concentrations. The concentration of the other two elements, Cr and Zn, is relatively lower (of the order of 1 and 0.1 ppm for a 15 $M_{\odot}$ model, 10 and 0.3 ppm for a 20 $M_{\odot}$ model, and 40 and 3 ppm for a 25 $M_{\odot}$ model).
5. For grains where measured concentrations of Fe and Ni are $\gtrsim$300 ppm, the implantation fraction is $\lesssim$0.25 and condensation dominates implantation, whereas for other grains, the implantation fraction can reach as high as $\sim$0.6. The implantation fraction of Ni is more than that of Fe, possibly due to Ni being more volatile and hence having higher chances of evaporation after condensation.

The free expansion phase is the time period of maximum activity in the newborn expanding ejecta; however, the quantity of implantation beyond this period (where temperature–distance equations become highly nonlinear) must be investigated to account for changes in the grain structure that may dominate those set by this phase. However, this may be less likely, since the grains might be able to develop protective layers of ice/organics or be embedded into larger grains, not to mention the decrement in density of particles due to the volumetric expansion of the ejecta, which will lead to a lower probability of interactions of grains with ions. In any case, studies on galactic chemical evolution should help solve these mysteries.

We are grateful to the anonymous referee whose comments helped improve this work. We acknowledge the utilization of the Vikram 100 HPC Supercomputing Facility at PRL, Ahmedabad, for computations related to SDTrimSP. We are indebted to Andreas Mutzke for his guidance while using SDTrimSP, Tuguldur Sukhbold for discussions on nucleosynthesis yields, and Arkaprabha Sarangi for discussions on SiC condensation.

We would also like to thank Sanjukta Dhar and Akarsh Relhan for running simulations on SDTrimSP. The project was funded by grant SERB-WE (964), Science and Engineering Research Board, Government of India.

Software: SDTrimSP (Mutzke et al. 2011), TRIM (Ziegler et al. 2009, 2010).

Appendix
Geometrical Considerations for Ion Transmission through the Grain

Here we describe the approximate geometrical model to calculate the fraction of ions transmitted through a spherical grain. Simulations in TRIM and SDTrimSP assume planar target surfaces, whereas we assume the grains to be spherical. This model backtraces the linear trajectory of a transmitted ion to a sphere inside the planar surface and finds the "extra" length such a transmitted ion has to travel in the planar surface as compared to a spherical one (see Section 3 for a discussion on the validity of linear trajectories). We perform this calculation of the extra lengths traversed for every ion that gets transmitted, and a weight equal to the ratio of extra length by total length traversed is assigned to each transmitted ion. The weights are calculated separately for each dimension and then multiplied. For example, if the weight (extra length) for an ion transmitted in the simulation comes as 1.05, it implies that 1.05 ions would have transmitted, had the surface been spherical.

Let us call the length $\overline{AC} = S_y$ (for y direction) and S_z (for z direction). A total of four cases are developed for each axis, such that each case in the region where y or $z > 0$ (called positive cases) has a corresponding case in the region where y or $z < 0$ (called negative cases). We note that $\theta \leqslant 135^{\circ}$ for positive cases; otherwise the ion path would not trace back to the sphere. Similarly, $45 < \theta < 180$ for negative cases. The y and z values have been limited to $\pm R$. We only discuss the first case as illustrated in Figure 4. The other three cases follow suit and can be worked on in a straightforward manner. For this case, $0 < \theta < 90$, $\theta > \beta$, z (or y) $\leqslant R$. Following the notations mentioned in Figure 4 and using the cosine angle formula, the

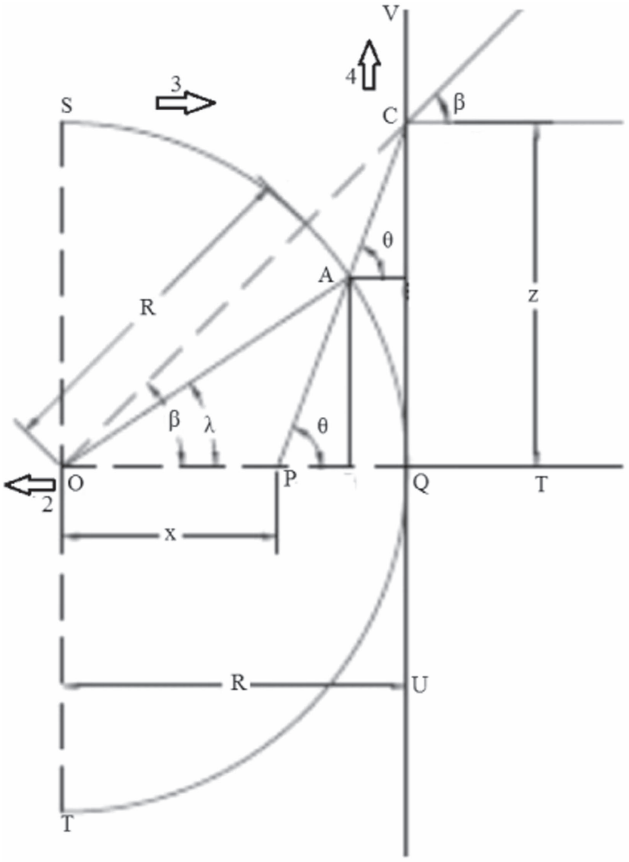

Figure 4. Depiction of the first case discussed in the Appendix on the geometric setup to find the fraction of incident ions transmitted through a spherical grain. Arrow 2 corresponds to the second case, when the trajectory of transmitted ion backtraces it to a point on the other side (LHS) of the center (i.e., point P lies on the LHS of center O). Arrow 3 depicts the third case where a highly oblique incident ion is transmitted (in the direction S–A–T), whereas arrow 4 portrays the fourth case where the ion transmitted cannot be traced back to the grain at all.

following equations can be derived for ΔOAC:

$$\angle OCA = \theta - \beta \tag{5}$$

$$\cos(\theta - \beta) = \frac{\overline{AC}^2 + \overline{OC}^2 - \overline{OA}^2}{2\,\overline{AC} \cdot \overline{OC}}. \tag{6}$$

Since $\overline{OC} = \sqrt{R^2 + z^2}$ and $\overline{OA} = R$,

$$\cos(\theta - \beta) = \frac{\overline{AC}^2 + z^2}{2\,\overline{AC} \cdot \sqrt{R^2 + z^2}} \tag{7}$$

$$\overline{AC} = \cos(\theta - \beta)\sqrt{R^2 + z^2} \pm \sqrt{(R^2 + z^2)\cos^2(\theta - \beta) - z^2} \tag{8}$$

The positive solution is to be discarded since $\beta > 0$ for our model. Thus

$$\overline{AC} = \cos(\theta - \beta)\sqrt{R^2 + z^2} - \sqrt{(R^2 + z^2)\cos^2(\theta - \beta) - z^2} \tag{9}$$

where $\overline{AC}$ is the extra length. Then the weight is given by

$$W = \frac{L_{py}}{L_{py} - S_y}\frac{L_{pz}}{L_{pz} - S_z}, \tag{10}$$

where L_{pi} is the length traversed in the planar target, measured from the center in the ith direction.

There are a few cases (specially at very oblique angles of incidence) wherein the particle gets transmitted owing to its crossing of the boundary of the target in only y or z direction. In such cases, the weights are computed as

$$W = \frac{L_{p(y,z)}}{L_{p(y,z)} - S_{(y,z)}}, \tag{11}$$

where the subscript (y, z) implies either y or z.

ORCID iDs

Kuljeet K. Marhas https://orcid.org/0000-0002-3375-3047
Piyush Sharda https://orcid.org/0000-0003-3347-7094

References

Amari, S., Anders, A., Virag, A., & Zinner, E. 1990, Natur, 345, 238
Amari, S., Hoppe, P., Zinner, E., & Lewis, R. S. 1992, ApJL, 394, L43
Amari, S., Lewis, R. S., & Anders, E. 1994, GeCoA, 58, 459
Amari, S., Lewis, R. S., & Anders, E. 1995, GeCoA, 59, 1411
Amari, S., Zinner, E., Clayton, D. D., & Meyer, B. S. 1998, M&PSA, 33, A10
Amari, S., Zinner, E., & Gallino, R. 2014, in AIP Conf. Ser. 1594, Origin of Matter and Evolution of Galaxies 2013: Proceedings of the 12th International Symposium on Origin of Matter and Evolution of Galaxies (OMEG12), ed. S. Jeong et al. (Melville, NY: AIP), 307
Arnett, D., Fryxell, B., & Mueller, E. 1989, ApJL, 341, L63
Aschenbach, B., Egger, R., & Trümper, J. 1995, Natur, 373, 587
Ávila, J. N., Ireland, T. R., Gyngard, F., et al. 2013, GeCoA, 120, 628
Biscaro, C., & Cherchneff, I. 2016, A&A, 589, A132
Borkowski, K. J., Blondin, J. M., & Sarazin, C. L. 1992, ApJ, 400, 222
Borkowski, K. J., Gwynne, P., Reynolds, S. P., et al. 2017, ApJL, 837, L7
Burbidge, E. M., Burbidge, G. R., Fowler, W. A., & Hoyle, F. 1957, RvMP, 29, 547
Cherchneff, I., & Dwek, E. 2009, ApJ, 703, 642
Chevalier, R. A. 2005, ApJ, 619, 839
Chevalier, R. A., Blondin, J. M., & Emmering, R. T. 1992, ApJ, 392, 118
Clayton, D. D. 1975a, ApJ, 199, 765
Clayton, D. D. 1975b, ApJ, 198, 151
Clayton, D. D., Arnett, D., Kane, J., & Meyer, B. S. 1997, ApJ, 486, 824
Clayton, D. D., Deneault, E. A.-N., & Meyer, B. S. 2001, ApJ, 562, 480
Clayton, D. D., Liu, W., & Dalgarno, A. 1999, Sci, 283, 1290
Clayton, D. D., Meyer, B. S., The, L.-S., & El Eid, M. F. 2002, ApJL, 578, L83
Deneault, E. 2017, ApJ, 843, 57
Deneault, E. A.-N., Clayton, D. D., & Heger, A. 2003, ApJ, 594, 312
Deneault, E. A.-N., Clayton, D. D., & Meyer, B. S. 2006, ApJ, 638, 234
Diehl, R., Parizot, E., Kallenbach, R., & von Steiger, R. 2013, in Proc. of the Two ISSI Workshops, The Astrophysics of Galactic Cosmic Rays, ed. R. Diehl (Netherlands: Springer)
Drake, R. P., Robey, H. F., Hurricane, O. A., et al. 2002, ApJ, 564, 896
Ebel, D. S., & Grossman, L. 2001, GeCoA, 65, 469
Fassia, A., Meikle, W. P. S., Geballe, T. R., et al. 1998, MNRAS, 299, 150
García, F., Suárez, A. E., Miceli, M., et al. 2017, A&A, 604, L5
Goel, P. S., & Murty, S. V. S. 1982, AdSpR, 2, 13
Grichener, A., & Soker, N. 2017, MNRAS, 468, 1226
Groopman, E. E. 2015, PhD thesis, Washington Univ.
Grossman, L., & Fedkin, A. V. 2013, M&PSA, 76, 5121
Gyngard, F., Amari, S., Zinner, E., & Ott, U. 2009, PASA, 26, 278
Haenecour, P., Floss, C., José, J., et al. 2016, ApJ, 825, 88
Hammer, N. J., Janka, H.-T., & Müller, E. 2010, ApJ, 714, 1371
Hashimoto, M., Nomoto, K., & Shigeyama, T. 1989, A&A, 210, L5
Heck, P. R., Hoppe, P., Gröner, E., et al. 2006, in 37th Annual Lunar and Planetary Science Conf., ed. S. Mackwell & E. Stansbery (Houston, TX: LPI), 1355
Heger, A., & Woosley, S. E. 2002, ApJ, 567, 532
Heger, A., & Woosley, S. E. 2010, ApJ, 724, 341
Henkel, T., Tizard, J., Blagburn, D., & Lyon, I. 2006, ApSS, 252, 7117
Hirashita, H., Nozawa, T., Asano, R. S., & Lee, T. 2016, P&SS, 133, 17
Hoppe, P. 2004, in ASP Conf. Ser. 309, Astrophysics of Dust, ed. A. N. Witt, G. C. Clayton, & B. T. Draine (San Francisco, CA: ASP), 265
Hoppe, P., Amari, S., Zinner, E., Ireland, T., & Lewis, R. S. 1994, ApJ, 430, 870

Hoppe, P., & Besmehn, A. 2002, ApJL, 576, L69
Hoppe, P., Leitner, J., Gröner, E., et al. 2010, ApJ, 719, 1370
Hoppe, P., Lodders, K., Fujiya, W., & Groener, E. 2014a, in 45th Lunar and Planetary Science Conf. (Houston, TX: LPI), 1031
Hoppe, P., Lodders, K., Strebel, R., Amari, S., & Lewis, R. S. 2001, ApJ, 551, 478
Hoppe, P., Pignatari, M., Fujiya, W., & Zinner, E. 2014b, in 77th Annual Meeting of the Meteoritical Society (Houston, TX: LPI), 5051
Hoppe, P., Strebel, R., Eberhardt, P., Amari, S., & Lewis, R. S. 2000, M&PS, 35, 1157
Horanyi, M., & Goertz, C. K. 1990, ApJ, 361, 155
Huss, G. R., Ott, U., & Koscheev, A. P. 2008, M&PS, 43, 1811
Hwang, U., Laming, J. M., Badenes, C., et al. 2004, ApJL, 615, L117
Janka, H.-T., & Mueller, E. 1996, A&A, 306, 167
Jerkstrand, A., Timmes, F. X., Magkotsios, G., et al. 2015, ApJ, 807, 110
Joggerst, C. C., Almgren, A., & Woosley, S. E. 2010, ApJ, 723, 353
Jones, A. P., Tielens, A. G. G. M., & Hollenbach, D. J. 1996, ApJ, 469, 740
Jones, A. P., Tielens, A. G. G. M., Hollenbach, D. J., & McKee, C. F. 1994, ApJ, 433, 797
Kane, J., Drake, R. P., & Remington, B. A. 1999, ApJ, 511, 335
Kashiv, Y., Cai, Z., Lai, B., et al. 2001, in 32nd Annual Lunar and Planetary Science Conf. (Houston, TX: LPI), 2192
Kashiv, Y., Cai, Z., Lai, B., et al. 2002, in 33rd Annual Lunar and Planetary Science Conf. (Houston, TX: LPI), 2056
Khokhlov, A. M., Höflich, P. A., Oran, E. S., et al. 1999, ApJL, 524, L107
Kifonidis, K., Plewa, T., Janka, H.-T., & Müller, E. 2003, A&A, 408, 621
Kirshner, R., Winkler, P. F., & Chevalier, R. A. 1987, ApJL, 315, L135
Knight, K. B., Sutton, S. R., Newville, M., et al. 2008, in 39th Lunar and Planetary Science Conf. (Houston, TX: LPI), 2135
Kobayashi, C., Umeda, H., Nomoto, K., Tominaga, N., & Ohkubo, T. 2006, ApJ, 653, 1145
Kodolányi, J., Stephan, T., Trappitsch, R., et al. 2017, GeCoA, in press
Kozasa, T., Hasegawa, H., & Nomoto, K. 1989, ApJ, 344, 325
Kudriavtsev, Y., Villegas, A., Godines, A., & Asomoza, R. 2005, ApSS, 239, 273
Kundt, W. (ed.) 1988, Supernova Shells and Their Birth Events (Vol. 316; Berlin: Springer)
Kuranz, C. C., Drake, R. P., Harding, E. C., et al. 2009, ApJ, 696, 749
Larimer, J. W., & Bartholomay, M. 1979, GeCoA, 43, 1455
Larsson, J., Fransson, C., Spyromilio, J., et al. 2016, ApJ, 833, 147
Lattimer, J. M., & Grossman, L. 1978, M&P, 19, 169
Lattimer, J. M., Schramm, D. N., & Grossman, L. 1978, ApJ, 219, 230
Lepp, S., Dalgarno, A., & McCray, R. 1990, ApJ, 358, 262
Levine, J., Savina, M. R., Stephan, T., et al. 2009, IJMSp, 288, 36
Lewis, R. S., Ming, T., Wacker, J. F., Anders, E., & Steel, E. 1987, Natur, 326, 160
Liu, N., Nittler, L. R., Alexander, C. M. O., & Wang, J. 2017, in 48th Lunar and Planetary Science Conf. (Houston, TX: LPI), 2331
Liu, N., Nittler, L. R., O'D Alexander, C. M., et al. 2016, ApJ, 820, 140
Lodders, K. 2003, ApJ, 591, 1220
Lodders, K. 2006, ApJL, 647, L37
Lodders, K., & Amari, S. 2005, ChEG, 65, 93
Lodders, K., & Fegley, B. 1997, in AIP Conf. Ser. 402, Astrophysical Implications of the Laboratory Study of Presolar Materials, ed. E. K. Zinner & T. J. Bernatowicz (Melville, NY: AIP), 391
Lodders, K., & Fegley, B., Jr. 1995, Metic, 30, 661
Lyon, I. C., Tizard, J. M., & Henkel, T. 2007, M&PS, 42, 373
Marhas, K. K., Amari, S., Gyngard, F., Zinner, E., & Gallino, R. 2008, ApJ, 689, 622
Marhas, K. K., Hoppe, P., & Ott, U. 2006, M&PSA, 41, 5248
Matsuura, M., Indebetouw, R., Woosley, S., et al. 2017, MNRAS, 469, 3347
Meyer, B. S. 1994, Metic, 29, 503
Meyer, B. S., Weaver, T. A., & Woosley, S. E. 1995, Metic, 30, 325
Müller, B., Melson, T., Heger, A., & Janka, H.-T. 2017, MNRAS, 472, 491
Mutzke, A., & Eckstein, W. 2008, NIMPB, 266, 872
Mutzke, A., Schneider, R., Eckstein, W., & Dohmen, R. 2011, SDTrimSP Version 5.0, IPP Rep. 12/8 (Garching: Max Planck Institute for Astrophysics)
Nadyozhin, D. K. 1994, ApJS, 92, 527
Nagataki, S. 2000, ApJS, 127, 141
Nagataki, S., Hashimoto, M.-a., Sato, K., & Yamada, S. 1997, ApJ, 486, 1026
Nittler, L. R., Amari, S., Zinner, E., Woosley, S. E., & Lewis, R. S. 1996, ApJL, 462, L31
Nomoto, K., Tominaga, N., Umeda, H., Kobayashi, C., & Maeda, K. 2006, NuPhA, 777, 424
Nozawa, T., Kozasa, T., & Habe, A. 2006, ApJ, 648, 435
Nozawa, T., Kozasa, T., Habe, A., et al. 2007, ApJ, 666, 955
Nozawa, T., Kozasa, T., Umeda, H., Maeda, K., & Nomoto, K. 2003, ApJ, 598, 785
Nuth, J. A., III 1988, in Meteorites and the Early Solar System (Tucson, AZ: Univ. of Arizona Press), 984
O'Connor, E., & Ott, C. D. 2011, ApJ, 730, 70
Pejcha, O., & Thompson, T. A. 2015, ApJ, 801, 90
Pignatari, M., Zinner, E., Hoppe, P., et al. 2015, ApJL, 808, L43
Pruet, J., Woosley, S. E., Buras, R., Janka, H.-T., & Hoffman, R. D. 2005, ApJ, 623, 325
Rauscher, T., Heger, A., Hoffman, R. D., & Woosley, S. E. 2002, ApJ, 576, 323
Rühm, W., Schneck, B., Knie, K., et al. 1994, P&SS, 42, 227
Saio, H., & Nomoto, K. 1988, Computational Astrophysics: Stellar Physics (New York: Springer)
Sarangi, A., & Cherchneff, I. 2013, ApJ, 776, 107
Sarangi, A., & Cherchneff, I. 2015, A&A, 575, A95
Sarkar, S., Niyogi, S., Bekyarova, E., & Haddon, R. C. 2013, arXiv:1308.4924
Sato, T., & Hughes, J. P. 2017, ApJ, 840, 112
Seward, F., Gorenstein, P., & Tucker, W. 1983, ApJ, 266, 287
Sharda, P., & Marhas, K. K. 2017, in 48th Lunar and Planetary Science Conf. (Houston, TX: LPI), 1490
Slavin, J. D., Jones, A. P., & Tielens, A. G. G. M. 2004, ApJ, 614, 796
Smartt, S. J. 2009, ARA&A, 47, 63
Smentkowski, V. S. 2000, PrSS, 64, 1
Smith, R. C., Kirshner, R. P., Blair, W. P., & Winkler, P. F. 1991, ApJ, 375, 652
Spicer, D. S., Maran, S. P., & Clark, R. W. 1990, ApJ, 356, 549
Steele, R. C. J., Coath, C. D., Regelous, M., Russell, S., & Elliott, T. 2012, ApJ, 758, 59
Sukhbold, T., Ertl, T., Woosley, S. E., Brown, J. M., & Janka, H.-T. 2016, ApJ, 821, 38
Sukhbold, T., Woosley, S., & Heger, A. 2017, arXiv:1710.03243
Suwa, Y., Tominaga, N., & Maeda, K. 2017, arXiv:1704.04780
Thielemann, F.-K., Hashimoto, M.-A., & Nomoto, K. 1990, ApJ, 349, 222
Thielemann, F.-K., Nomoto, K., & Hashimoto, M.-A. 1996, ApJ, 460, 408
Tielens, A. G. G. M., McKee, C. F., Seab, C. G., & Hollenbach, D. J. 1994, ApJ, 431, 321
Todini, P., & Ferrara, A. 2001, MNRAS, 325, 726
Trappistch, R., Stephen, T., Savina, M. R., et al. 2017, GeCoA, in press
Travaglio, C., Gallino, R., Amari, S., et al. 1999, ApJ, 510, 325
Truelove, J. K., & McKee, C. F. 1999, ApJS, 120, 299
Utrobin, V. P., & Chugai, N. N. 2017, MNRAS, 472, 5004
Utrobin, V. P., Wongwathanarat, A., Janka, H.-T., & Müller, E. 2015, A&A, 581, A40
Verchovsky, A. B., Fisenko, A. V., Semjonova, L. F., et al. 1998, Sci, 281, 1165
Verchovsky, A. B., Wright, I. P., & Pillinger, C. T. 2003, M&PSA, 38, 5200
Verchovsky, A. B., Wright, I. P., & Pillinger, C. T. 2004, ApJ, 607, 611
Vyšinka, M., Vaverka, J., Pavlu, J., Nemecek, Z., & Šafránková, J. 2009, in Proc. of the 18th Annual Conf. of Doctoral Students—WDS 2009, Part II, ed. J. Šafránková & J. Pavlů, 195
Wanajo, S., Müller, B., Janka, H.-T., & Heger, A. 2018, ApJ, 852, 40
Weaver, T. A., Zimmerman, G. B., & Woosley, S. E. 1978, ApJ, 225, 1021
Wittmaack, K., & Mutzke, A. 2012, NIMPB, 281, 37
Wongwathanarat, A., Janka, H.-T., & Müller, E. 2013, A&A, 552, A126
Wongwathanarat, A., Janka, H.-T., Müller, E., Pllumbi, E., & Wanajo, S. 2017, ApJ, 842, 13
Wongwathanarat, A., Müller, E., & Janka, H.-T. 2015, A&A, 577, A48
Wooden, D. H. 1997, AIP Conf. Ser. 402, Astrophysical Implications of the Laboratory Study of Presolar Materials, ed. T. J. Bernatowicz & E. Zinner (Melville, NY: AIP), 317
Woosley, S. E., & Heger, A. 2007, PhR, 442, 269
Woosley, S. E., Heger, A., & Weaver, T. A. 2002, RvMP, 74, 1015
Woosley, S. E., & Weaver, T. A. 1986, ARA&A, 24, 205
Woosley, S. E., & Weaver, T. A. 1995, ApJS, 101, 181
Yin, Q.-Z., Lee, C.-T. A., & Ott, U. 2006, ApJ, 647, 676
Yoshida, T. 2007, ApJ, 666, 1048
Yu, T., Meyer, B. S., & Clayton, D. D. 2013, ApJ, 769, 38
Ziegler, J., Biersack, J., & Littmark, U. 2009, SRIM—The Stopping and Ranges of Ions in Matter (Oxford: Pergamon) Revised Edition
Ziegler, J. F., Ziegler, M. D., & Biersack, J. P. 2010, NIMPB, 268, 1818
Zinner, E. 1998, AREPS, 26, 147
Zinner, E., Amari, S., Guinness, R., et al. 2007, GeCoA, 71, 4786
Zinner, E., Jadhav, M., Gyngard, F., & Nittler, L. R. 2011, in 42nd Lunar and Planetary Science Conf. (Houston, TX: LPI), 1070